Research Paper

Improving the Estimation of the Impact of the IOD-Modulated MJO on the Autumnal Precipitation Variability over Iran by Simultaneously Utilizing the RMM and RM-RMM Indices

Sharifoddin Mansouri

Assistant Prof. of Communication Systems, Department of Electrical Engineering, Marvdasht Branch, Islamic Azad University, Marvdasht, Iran

Received: 2025/03/15
Revised: 2025/04/05
Accepted: 2025/10/29

Use your device to scan and read the article online

DOI:
10.71632/wej.2025.1167458

Keywords:
RMM index, RM-RMM index, IOD state, bootstrap method, false discovery rate

Abstract

Introduction: In the present study, owing to the substantial effect of the Indian Ocean Dipole (IOD) on the activity of the Madden-Julian Oscillation (MJO), the focus is on improving the estimation of the influence of the IOD on the MJO-related precipitation variabilities over Iran during the October-to-November (ON) periods which coincide with the peak activity of the IOD.

Methods: This is achieved by comparing the corresponding active phases of the Real-time Multi-variate MJO (RMM) and Regionally Modified RMM (RM-RMM) indices during the Positive, Neutral and Negative IOD events, separately. Accordingly, in addition to performing a localized significance test at each grid point, the field significance of these tests was also assessed within the study region, Iran, by using the False Discovery Rate (FDR) method.

Findings: The significant positive (negative) differences in the precipitation anomaly and occurrence probability are detected during the phases 8 and 1 (phase 4) of the RM-RMM and RMM indices over some parts of Iran, during the Positive IOD (Negative) IOD event which intensifies the MJO's convection (suppression) and the lower-level convergence (divergence) of the moisture over the western Indian Ocean. However, during the Neutral IOD event no significant precipitation difference between the pertinent phases is observed. These findings suggest that by forecasting the interannual variations in the IOD and anticipating the associated precipitation differences between the equivalent phases of the RM-RMM and RMM indices, there is potential to increase the accuracy of the precipitation forecasts for Iran.

Citation: Mansouri S. Improving the Estimation of the Impact of the IOD-Modulated MJO on the Autumnal Precipitation Variability over Iran by Simultaneously Utilizing the RMM and RM-RMM Indices. Water Resources Engineering Journal. 2025; 18(66): 69- 90.

Corresponding author: Sharifoddin Mansouri
Address: Department of Electrical Engineering, Marvdasht Branch, Islamic Azad University, Marvdasht, Iran
Tell: +989173148927
Email: mv.sharifoddin@iau.ac.ir

Extended Abstract

Introduction

The previous studies have examined the combined influence of the MJO, a major tropical weather pattern which influences the intra-seasonal variabilities of the global climate via teleconnections, and, the IOD, a key climate driver that modulates the MJO's dynamics, on the precipitation in Iran. However, this study is the first to compare how the RMM index and the regionally-tailored RM-RMM index capture the influence of the IOD-modulated MJO on the Iran's rainfall.

Materials and Methods

This research concentrates on the October-to-November period, when the IOD is at its peak and significantly correlates with Iran's precipitation, unlike the El-Niño Southern Oscillation (ENSO) phenomenon. Before calculating the anomalies of each climatic variable (the high-resolution daily precipitation as well as the global atmospheric data, 1979-2022) a 5-day running mean is applied to its data to filter out the high-frequency noise. In this regard, the precipitation patterns over Iran during the equivalent phase numbers of the RMM and RM-RMM indices across different IOD events are compared, separately. At each grid point, the local significance of the anomalies (or the differences of the anomalies) is then tested by using a bootstrap resampling method. Finally, the global significance of the relevant atmospheric composite is assessed by the FDR method.

Findings

The significant differences in the precipitation anomaly as well as the precipitation occurrence probability between the corresponding phases of the RM-RMM and RMM indices are revealed over Iran during the Positive IOD (phases 1 and 8 of the MJO, separately) and the Negative IOD (phase 4 of the MJO) events. However, no significant differences in the precipitation variations between the equivalent phases of the two indices are observed across the country during the Neutral IOD event.

Discussion

During the Positive IOD (hereafter, +IOD) event, the convergence of the moisture at the lower troposphere and enhancement of the convection activity of the MJO due to the positive SST anomaly over the western Indian Ocean result in an increase in the precipitation variations in this region during the phases 8 and 1 of the MJO. The 14° eastward phase-shift of the RM-RMM phase (relative to the RMM index) allows it to capture this enhanced activity more effectively than the RMM index.

Accordingly, due to the cloudiness, uplift of the air, cyclonic advection of the moisture and sharpened exit-region of the upper-level jet, the precipitation anomaly (occurrence probability) increases by 0.1 to 1.5 mm (0.08 to 0.28) in the western, central, southern, southeastern and northeastern Iran, and, on the southwestern, southern and southeastern coasts of the Caspian Sea, during the phase 8 of the RM-RMM in comparison with that of the RMM. On the contrary, in a small area on the northeastern boundary of Iran, the air descent and moisture divergence lead to a decrease in the precipitation anomaly (occurrence probability), which is about 0.8 mm (0.2).

In addition, the existence of a significant VIMF anomaly, air ascent, and intensification of the jet at the upper troposphere, increase the precipitation anomaly (occurrence probability) by 1 mm (0.28) over the Zagros Mountains in the northwestern Iran, during the phase 1 of the RM-RMM index compared to the phase of the RMM. However, the lack of a significant VIMF anomaly causes a decrease in the precipitation anomaly (occurrence probability), ranging from 0.1 to 1 mm (0.06 to 0.21), on some small parts in the southern, eastern and northeastern Iran, during the RM-RMM phase 1 with respect to the RMM phase 1.

On the other hand, during the Negative IOD (hereafter, -IOD) event, the negative SST anomaly weakens the MJO's convection over the western Indian Ocean. Moreover, the divergence of the moisture at the lower troposphere on this region takes place.

These factors might result in a decrease in the precipitation anomaly during the phase 4 (dry phase) of the MJO over the southwestern Asia. The RM-RMM index captures this signal more effectively than the RMM index due to its 14° eastward phase-shift. In this manner, the air subsidence and the lack of a significant VIMF anomaly decreases the precipitation anomaly by 0.1 to 0.2 mm over the southwestern Iran, during the RM-RMM phase 4 relative to the RMM phase 4. However, due to the intensification of the sub-tropical jet in the vicinity of the regions, over which the significant moisture anomaly and local moisture convergence exists, the precipitation anomaly (occurrence probability) increases by 0.2 to 0.6 mm (0.07 to 0.25) over the Zagros Mountains in the western Iran, during the phase 4 of the RM-RMM index compared to that of the RMM.

Conclusion

In conclusion, these findings suggest that by predicting the interannual variations of the IOD, and considering the significant differences between the corresponding phases of the RM-RMM and RMM indices, the estimation of the influence of IOD on the MJO-related precipitation over Iran might be ameliorated. In other words, there is potential for enhancing the accuracy of the long-range precipitation forecasts.

Funding

No funding.

Conflicts of interest

The author declares no conflict of interest.

1. Introduction

The MJO is the primary mode of the intra-seasonal variability in the tropical regions, which is characterized by eastward-propagating motion (1) that includes large-scale circulation patterns and convective clouds moving from the tropical western Indian Ocean toward the central equatorial Pacific over a span of 30 to 60 days. The upper-tropospheric diabatic heating above the center of the convective activity of the MJO transmits the Rossby waves to the extra-tropical regions, which influence the intra-seasonal climate variabilities in these areas. This phenomenon is known as the teleconnection effect of the MJO (2, 3, 4, 5). Conversely, the winds which flow from the extra-tropics to the tropics impact the onset or intensity of the MJO (6, 7). Moreover, the MJO affects the Northern Hemisphere extra-tropical variables with a delay of one or two weeks (8, 9).

The RMM index, introduced by Wheeler and Hendon (10), monitors the MJO's convective activities and circulation patterns by using the OLR (the Outgoing Longwave Radiation), which indicates the cloudiness, and, the U850, and U200 (the velocity of the zonal wind at the 850 and 200 hPa, respectively), which represent the air circulation. This index, which divides the motion of the MJO into eight distinct phases within the tropical regions, has been successfully employed to explore the impacts of the MJO on various variables across different geographical locations (11, 12, 13). In a recent study, Mansouri et al. (14) introduced the RM-RMM index, which improves the estimation of the influence of the MJO on the precipitation variation over Iran during the boreal cold months, when more than 75% of the annual precipitation occurs across the country (15), To be more precise, in comparison to solely relying on the RMM index, the simultaneous utilization of both the RMM and RM-RMM indices reveals significant differences in the estimates of the MJO-related precipitation variabilities over Iran between the corresponding phases of the two indices.

In addition, approximately 40% of the MJO events originate from the western equatorial region of the Indian Ocean (16), with peak convective activity in the Indo-Pacific warm pool region (1). Consequently, any changes in the MJO behavior within the Indian Ocean might lead to the significant global intra-seasonal variations. The gradient of the Sea Surface Temperature (SST) anomaly between the western and eastern tropical zones of the Indian Ocean is a key driver, which affects the MJO's dynamics in this region (17, 18, 19), varies interannually across the equatorial Indian Ocean. This phenomenon, which is known as the IOD, is characterized by a *bipolar* structure (20). The IOD phenomenon begins to develop in the summer season of the northern hemisphere; it reaches its maximum in the autumn; and its activity diminishes and disappears in the winter. Moreover, the index associated with the activity of the IOD is referred to as the Dipole Mode Index (DMI), which is calculated from the difference in the SST anomaly between the western and southeastern tropical Indian Ocean (20). Subsequently, the state of the IOD is classified into one of the three events: the +IOD, the -IOD, or the Neutral IOD, based on the sign and magnitude of the DMI. During the +IOD event, the negative and positive SST anomalies occur over the eastern Indian Ocean (near Sumatra) and the western part of this ocean, respectively (20).

During the occurrence of the +IOD phenomenon, the easterlies of the horizontal wind anomaly attenuate the westerlies of the horizontal wind anomaly at the lower troposphere over the equatorial Indian Ocean and reduce the period of the MJO (21). The opposite happens during the -IOD event. Notably, that various studies have investigated the impact of the IOD on the intra-seasonal variabilities in the Indian Ocean (19, 22, 23).

It is worth mentioning that the ENSO phenomenon might also affect the MJO's activity in the Indian Ocean. However, the IOD stands out as the most influential phenomenon in this context (24). To be more precise, Wilson et al. (19) have shown that by removing the effect of the ENSO from the intra-seasonal OLR and U200 data over the western Indian Ocean, the correlation between this data and the DMI index remains relatively unchanged when compared to the situation where the impact

of the ENSO is not eliminated. On the other hand, the same analysis reveals that the impacts of the IOD and ENSO phenomena on the intra-seasonal U850 data are almost equally significant. In conclusion, it can be asserted that in the Indian Ocean the IOD significantly influences the intra-seasonal variabilities used in the calculation of the MJO index. Furthermore, during the El Niño events (positive ENSO phases), the impact of the +IOD is enhanced on the MJO. In contrast, during the La Niña events (negative ENSO phases), the effect of the -IOD on the MJO becomes more pronounced (19).

Due to the fact that the area of interest in this research (Iran) is in the southwestern Asia, which is located in the western Indian Ocean, studying the effect of the IOD on the climatic variations over this region is of great importance. Numerous studies have probed either the impacts of the IOD-modulated MJO on the precipitation over Iran during the boreal cold months (17, 18, 24), or the direct influence of the IOD on the precipitation over the country and its neighboring regions during the autumn and/or early winter (25, 26, 27). However, none of them have shed light on the distinctions in the effect of the IOD-modulated MJO on the climate variables over the country from the perspective of the two MJO indices, RMM and RM-RMM, during the boreal autumn when the activity of the IOD reaches its maximum. Albeit, it is noteworthy that the activity of the MJO is slightly weaker during this season in comparison to the boreal winter (19, 28). Nevertheless, a significant correlation is observed between the IOD and the precipitation variabilities over Iran during the boreal autumn, while the corresponding correlation between the ENSO and the precipitation over the country is not significant (26).

Accordingly, this research aims to investigate the influence of the MJO events on Iran during various IOD occurrences, during the October-to-November periods. In this regard, the precipitation patterns over Iran during the equivalent phase numbers of the RMM and RM-RMM indices across different IOD events are compared, separately. The following sections of this paper provide further details: Section 2 describes the data and methodology, Section 3 presents the results and discussion, and Section 4 offers a summary and conclusion.

2. Data and methods

2.1 Generating the Spatial Distributions of Different Anomalies and Determining Their Statistical Significance

For investigating the advantage of the RM-RMM index over the RMM in estimating the MJO-related precipitation on Iran, Mansouri et al. (14) used the daily precipitation data based on the CPC integrated gauge-based precipitation dataset with a spatial resolution of 0.5° longitude (29). Here, to compare the results with those of the previous study, the same data was gratefully obtained from the NOAA website. It is noteworthy that although some higher-resolution datasets exist, the CPC integrated gauge-based precipitation dataset still possesses an acceptable resolution. Additionally, as stated later in the text, the data used to calculate the MJO index has been downloaded from the NOAA website (10). Other data has also been downloaded from the NOAA website to avoid issues such as inconsistencies among the data from different sources, the need for preprocessing to harmonize them, and cross-validation challenges -except for the yearly IOD data, which has been downloaded from the Australian Bureau of Meteorology website.

For analyzing the large-scale atmospheric circulation, the daily NCEP/NCAR reanalysis data, which includes the geopotential height at 700 and 200 hPa (H200 and H700) levels, the vertical velocity (omega) at the 500 hPa level, and the horizontal wind velocity and the specific humidity at various pressure levels, at a spatial resolution of 2.5˚ latitude-longitude was downloaded from the NOAA website with gratitude (30). Furthermore, to examine the overall sources and sinks of the regional moisture, the Vertically Integrated Moisture Flux (VIMF) was computed using the following equation:

$$\mathbf{Q} = \frac{1}{g}\int_{1000}^{300} q\mathbf{v}\ dp \qquad (1)$$

where g represents the gravitational acceleration, q is the specific humidity, **v** denotes the horizontal wind velocity vector,

and **Q** stands for the VIMF. The lower and upper bounds of the integral correspond to the pressure levels of 1000 and 300 hPa, respectively. Finally, to study the average convergence or divergence of the moisture flux, the divergence of the moisture flux was integrated vertically to compute the VIMFD.
Moreover, all of this data was downloaded for the period from 1 January 1979 to 31 December 2022. Additionally, in the process of calculating the anomaly for each variable, a 5-day moving average filter was initially applied to the data of that particular variable to mitigate the effects of synoptic (high-frequency) variability, as suggested by Krishnamurthy and Shukla (31). Following this step, the long-term daily climatology was calculated and subtracted from the filtered results. Subsequently, this anomaly was utilized to generate the spatial patterns for that variable.
It is worth noting that at each grid point, to detect the local significance of the (average) anomalies of a certain variable in a predetermined set of times, the bootstrap resampling method was used, which is independent of the data distribution (11). To be more precise, 10,000 subsets were randomly selected from this predetermined set of the anomalies, the number of the members of each of them was equal to that of the predetermined set. Then by choosing a suitable test statistic, for example a pivot statistic, the value of the test statistic was calculated for each of the randomly selected subsets, separately. Then, by sorting these 10,000 calculated statistics from small to large and using a two-sided test, the statistical significance of the (average) anomalies of the specified variable was evaluated at a required level (here 0.05 unless otherwise stated). In a similar manner, this process was used for the statistical significance of the difference between (the averages of) two sets of anomalies of a certain variable (32).
On the other hand, at each grid point, the probability of the precipitation occurrence in a specific set of time instances was calculated by dividing the number of wet days (days on which the 5-day moving average of the total precipitation exceeded 1 mm/day) by the total number of the members in that set. Furthermore, by assigning "1" to the wet days and "0" to the other days of that set, the statistical significance of this occurrence probability was determined using the bootstrap resampling method. Similarly, this method could judge the statistical significance of the difference in the occurrence probability of the precipitation between two predetermined sets of times.
After conducting a localized significance test at each grid point, the field significance of these multiple hypothesis tests was also assessed within the study region (Iran) using the FDR method to restrict the rate of the false rejections of the zero hypotheses (33, 34, 35). In this approach, some suitable values were initially selected for the significance level of the global hypothesis test (α_{Global}) and the upper bound of the expected ratio of the local null hypotheses which were falsely rejected in the study area (α_{FDR}). Then, at each grid point, the desired test statistic (observed statistic) was calculated using the predetermined set of anomalies. Following this, by assuming that the null hypothesis was valid at each point, an empirical distribution of the test statistic was generated using the bootstrap resampling method. Subsequently, an estimate of the p-value was obtained as the fraction of those test statistics whose absolute values exceeded that of the observed statistic (32). Finally, the p-values of all grid points were sorted in the ascending order ($p_1 \leq p_2 \leq \cdots \leq p_N$) and a threshold value named p_{FDR} was selected according to Equation 2:

$$p_{FDR} = \max \{ p_i : \ p_i \leq \left(\frac{i}{N}\right) \alpha_{FDR} \} \qquad (2)$$

Here N represents the total number of grid points and i = 1, 2, ..., N. The grid points with p-values not exceeding p_{FDR} were considered as significant points, representing the rejection of the local null hypothesis at these locations. Consequently, the presence of these statistically significant points in the region indicated the rejection of the global null hypothesis or the global (field) significance in that region. Furthermore, the value of α_{Global} was set at 0.05. However, instead of using the same value for α_{FDR}, a value of approximately 0.10 was chosen for it due to the high spatial correlation among the data of each variable

Table 1- Various IOD events during the years 1979 to 2022 obtained from the Australian Bureau of Meteorology.

+IOD	1994, 1997, 2006, 2015, 2019
Neutral	1979, 1980, 1981, 1982, 1983, 1984, 1985, 1986, 1987, 1988, 1989, 1991, 1993, 1995, 1999, 2000, 2001, 2002, 2003, 2004, 2005, 2007, 2008, 2009, 2011, 2012, 2013, 2014, 2017, 2018, 2020, 2021
-IOD	1990, 1992, 1996, 1998, 2010, 2016, 2022

in the study area, as described by Gloeckler and Roundy (36), Ventura et al. (33), and Wilks (35). It is worth noting that the FDR approach was solely applied to the precipitation anomalies and precipitation occurrence probabilities. For the anomalies of other variables, only a local significance test was conducted by utilizing the bootstrap resampling method.

2.2. The IOD Index (DMI)

The Indian Ocean DMI is calculated from the difference in the SST anomaly between the western Indian Ocean (50˚E-70˚E and 10˚S-10˚N) and the eastern Indian Ocean (90˚E-110˚E and 0˚-10˚S). Subsequently, the state of the IOD is identified as one of the +IOD, -IOD or Neutral IOD events. Based on this, the state of the IOD in different years was gratefully obtained from the website of the Australian Bureau of Meteorology (http://www.bom.gov.au/climate/iod/). Table 1 represents the years in which this dipole is in its positive, neutral, or negative phases.

2.3 Recomputing the RMM and RM-RMM Indices by Employing the Relevant Data

In addition to the daily NCEP/NCAR reanalysis U850 and U200 data (30), the interpolated OLR data, which indicates the cloudiness, precipitation and convective activity (37), was thankfully downloaded from the website of NOAA. This data was acquired at a spatial resolution of 2.5˚ latitude-longitude and covers the period from 1 January 1979 to 31 December 2022.

In order to reproduce the RMM and RM-RMM indices using the methodology of Gottschalck et al. (38), the initial step involved removing the seasonal cycle (the mean over time and the first three harmonics of the annual cycle) the raw data of the above-mentioned variables. Following this, the deseasonalized data of each variable were subjected to the subtraction of the previous 120-day running mean to extract the intra-seasonal anomalies. Subsequently, the intra-seasonal anomalies of each variable were averaged across all longitudes from 15˚S to 15˚N, except for the longitudes spanning from 30˚E to 60˚E in the RM-RMM case, where the averaging extended from 15˚S to 35˚N (14, 38). Following this preprocessing stage, the mean anomalies of each variable, based on their longitudes, were arranged in the columns of a matrix known as the *anomaly matrix* of the specified index. It is noteworthy that the variances of the 30˚E-60˚E columns of the RM-RMM anomaly matrix were, on average, lower than those of the RMM anomaly matrix (See Fig. 2 of 14). The next step involved calculating the *global* variance of the anomalies for each variable, which is the average of the variances of the columns of the anomalies associated with that variable in the anomaly matrix. Subsequently, the columns of the anomalies of each variable were normalized by the square root of their respective global variance. Finally, the Empirical Orthogonal Functions (EOFs) of the anomaly matrix of the specified index were computed, and the Principal Components (PCs) corresponding to the first two of these EOFs constituted the RMM (RM-RMM) index.

The RMM index is depicted in a two-dimensional phase space, which serves as a tool to visualize the spatial and temporal evolution of the MJO. Moreover, the eastward propagation of the MJO along the equator is divided into eight distinct phases, with each phase being assigned a *phase number* ranging from 1 to 8. These phase numbers are defined based on the

geographical location of the center of the convective activity (enhanced precipitation) of the MJO over various regions: the western hemisphere and Africa (phase numbers 8 and 1), the Indian Ocean (phase numbers 2 and 3), the Maritime Continent (phase numbers 4 and 5), and the western Pacific Ocean (phase numbers 6 and 7). Ultimately, whenever the amplitude of the RMM index exceeds 1 the associated MJO phase number is classified as *active*; otherwise, it is considered as *inactive* regardless of the phase in the MJO cycle. In a similar manner, the *RM-RMM* index is also represented in its two-dimensional phase space. It is noteworthy that the correlations between the corresponding components of the RMM and RM-RMM indices are greater than 95%, which indicates a strong resemblance between these two indices. As a result, the leading EOFs of the RM-RMM index were not deliberately realigned to coincide with those of the RMM (14). In addition, on average, the phase of the RM-RMM index lags the RMM index by approximately 14 degrees. This 14° phase difference between the RMM and RM-RMM indices forms the foundation for comparing the influence of the MJO phenomenon with the combined impacts of the intra-seasonal variabilities in the tropics-Southwest Asia on the precipitation over Iran (14).

Furthermore, by considering the *concurrently active* phases of both indices, it is observed that in over 97% of the cases, when the RMM index is in a specific phase number, the RM-RMM index is either in the same phase number or in the preceding one. For instance, when the RMM index is in the phase number 7, the concurrently active phase number of the RM-RMM index, due to its phase-lag compared to the RMM index, will be either 7 or 6 (refer to Fig. 3 in 14).

Moreover, every (active) phase number of each index can be divided into two sub-phases: *in-phase* and *out-of-phase*. Consequently, in the aforementioned example, the sub-phases of the phase number 7 of the RMM index are represented as 7_7 (in-phase with the RM-RMM index) and 6_7 (out-of-phase with the RM-RMM index). In each of these representations, the number *preceding* the '_' denotes the corresponding phase number of the RM-RMM index, while the number *following* the '_' represents the associated phase number of the RMM index. As another example, the phase number 7 of the RM-RMM index is subdivided into the 7_7 (in-phase with the RMM index) and 7_8 (out-of-phase with the RMM index) sub-phases. Similarly, other concurrently active phase numbers of the RMM and RM-RMM indices can be subdivided into the in-phase and out-of-phase sub-phases. An application of these sub-phases will be described in Sub-Section 2.4.

Furthermore, the spatial distributions of the average and the standard deviation of the total precipitation over the country during the ON months of 1979-2022 are depicted in Fig. 1a and Fig. 1b, respectively. In Fig. 1 the average (standard deviation) of the total precipitation on the western, northwestern, northern and northeastern boundaries of Iran ranges from 0.3 to 6 (0.6 to 9) mm/day. Conversely, the central and southern parts of the eastern half of the country experience an average (a standard deviation) of less than 0.3 (0.6) mm/day during the ON months. This discrepancy is due to the presence of the mountains in the northern and western Iran (Alborz and Zagros Mountains, respectively), which affect the distribution of the precipitation variabilities over the country significantly (39). On the other hand, over two deserts, which are located in the central and southern parts of the eastern Iran, the total precipitation is lower compared to the mountainous areas. As the climate of Iran is classified as semi-arid and arid, the water resources, agricultural yields, and the regional economy are highly susceptible to the severe droughts (26, 40). Accordingly, even during the ON months, which accounts for less than 25% of the annual precipitation, it is important to assess

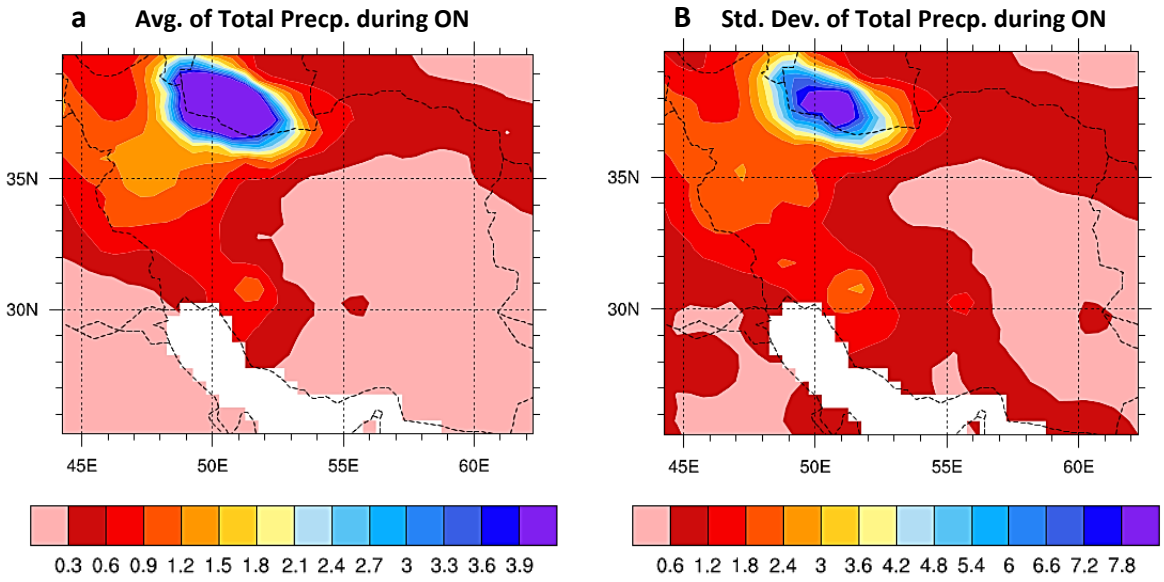

Fig. 1- Spatial patterns of the precipitation during the boreal autumn season of 1979-2022 over Iran, (a) average of the total precipitation (mm/day), and (b) standard deviation of the total precipitation (mm/day)

the impact of the MJO on the precipitation over this country.

2.4. Detecting the Significant Differences in the Impact of the IOD-Modulated MJO on Various Climate Variables between the Corresponding Phase Numbers of the RMM and RM-RMM Indices

By taking into account the influence of the IOD on the MJO and on the tropics-Southwest Asia intra-seasonal variabilities, to examine the distinctions in the impacts of these two IOD-modified phenomena on the precipitation and other climate variables over Iran, only the concurrently active phase numbers of the RM-RMM and RMM indices were considered. Subsequently, the spatial distributions of various anomalies were constructed for each active phase number of the RM-RMM and RMM indices during the +IOD, -IOD, and Neutral IOD events, separately. Then, during each of these IOD events, the significant differences between the spatial distributions of the anomalies pertinent to the equal phase numbers of the RM-RMM and RMM indices were identified, using a test statistic according to Guo and Yuan (41), and Mansouri et al. (14):

$$T_{weighted} = \sqrt{\gamma}\,\frac{\bar{X}_{1,U} - \bar{X}_{2,U}}{\sqrt{\frac{S^2{}_{1,U}}{n_1} + \frac{S^2{}_{2,U}}{n_2}}} + \sqrt{1-\gamma}\,\frac{\bar{D}}{S_D/\sqrt{n}} \quad (3)$$

It is noteworthy that this test statistic is appropriate for detecting the differences in the mean anomaly between two partially overlapping sets of samples, which is the case for the equal phase numbers of the RM-RMM and RMM indices (as explained in Sub-Section 2.3, the equal phase numbers of the RM-RMM and RMM indices exhibit a combination of both in-phase and out-of-phase characteristics with each other). In Formula 3, for comparing the means of the two predetermined sets of anomalies, n_1 and n_2 represent the number of samples in the out-of-phase parts of the first and second sets, respectively; while, n denotes the number of samples in the in-phase parts of the two sets. Moreover, $\bar{X}_{1,U}$ and $S_{1,U}$ ($\bar{X}_{2,U}$ and $S_{2,U}$) are respectively the mean and the standard deviation of the out-of-phase part of the first (second) set. Additionally, $\bar{D}$ and S_D are the mean and the standard deviation of the differences between the in-phase parts of the two specified sets, respectively. Finally, γ stands for the proportion of the out-of-phase samples, defined as $\gamma = (n_1 + n_2)/(n_1 + n_2 + n)$.

Table 2- The number of the days of the RM-RMM and RMM concurrently active phases, as well as the days of each in-phase sub-phase during the +IOD event during the ON months of 1979-2022

RM-RMM phases	1: 62	2: 39	3: 20	4: 4	5: 9	6: 6	7: 10	8: 86
RMM phases	1: 83	2: 51	3: 22	4: 3	5: 10	6: 6	7: 7	8: 54
in-phase sub-phases	1_1: 47	2_2: 36	3-3: 19	4_4: 2	5_5: 8	6_6: 5	7_7: 6	8_8: 50

Table 3- As in Table 2, but during the -IOD event

RM-RMM phases	1: 31	2: 8	3: 12	4: 38	5: 62	6: 46	7: 34	8: 22
RMM phases	1: 31	2: 9	3: 10	4: 31	5: 66	6: 48	7: 32	8: 26
in-phase sub-phases	1_1: 27	2_2: 6	3_3: 8	4_4: 27	5_5: 55	6_6: 41	7_7: 27	8_8: 18

Table 4- As in Table 2, but during the Neutral IOD event

RM-RMM phases	1: 148	2: 125	3: 96	4: 185	5: 211	6: 156	7: 98	8: 139
RMM phases	1: 139	2: 132	3: 99	4: 170	5: 205	6: 171	7: 106	8: 126
in-phase sub-phases	1_1: 115	2_2: 99	3_3: 73	4_4: 147	5_5: 167	6_6: 127	7_7: 77	8_8: 105

Accordingly, during the ON months from 1979 to 2022, the number of the days for every active phase of both the RM-RMM and RMM indices, as well as the days for each in-phase sub-phase were computed. Tables 2 to 4 indicate this data separately for the +IOD, -IOD, and Neutral IOD events.

Table 2 (Table 3) represents that during the +IOD (-IOD) event the number of the days increases during the MJO phases 1 and 8 (4, 5 and 6). These phases are located in the western (eastern) Indian Ocean, where the +IOD (-IOD) enhances the MJO's convection and circulation. Moreover, in Table 2 (Table 3), during the +IOD (-IOD) event, the maximum difference in the number of days between the corresponding phases of the RM-RMM and RMM indices with respect to their average is observed during the phases 1 and 8 (during the phase 4), which are respectively 21/73.5 and 32/70 (which is 7/34.5).

It is noteworthy that the Neutral IOD event resembles the -IOD event in the maximum number of the days during each MJO phase (Table 4). However, due to the existence of weaker IOD events in this period, the relative difference between the corresponding phases of the RM-RMM and RMM indices are not as large as those during the -IOD events.

3. Results and Discussion

By aiming a more precise assessment of the influence of the IOD-modulated MJO on the precipitation patterns in Iran, the spatial distribution of the anomalies of each meteorological field during every active phase of the RM-RMM index was compared with that during the corresponding active phase of the RMM index. This comparison was conducted separately for each of the +IOD, -IOD and Neutral IOD events. In a similar manner, the significant differences in the precipitation occurrence probability

between the relevant phases of the two indices were also sought during each of the above-mentioned IOD events. It is worth noting that those comparison cases in which no global significant difference was observed in both the precipitation anomaly and the precipitation occurrence probability between the corresponding phases of the RM-RMM and RMM indices have been eliminated. For instance, during the -IOD event, the difference in the precipitation anomaly and in the precipitation occurrence probability were not globally significant between any of the equal active phase numbers of the RM-RMM and RMM indices. Therefore, none of these differences were depicted.

3.1. The Distinctions in the Spatial Distributions of Various Anomalies between the Corresponding Phases of the RM-RMM and RMM Indices during +IOD Events

Fig. 2 illustrates the significant differences in various anomalies between the phase 1 of the RM-RMM index and the phase 1 of the RMM index, during the +IOD event. In Fig. 2a, no significant difference in the OLR anomaly is observed over Iran, which indicates that no distinction in the cloudiness occurs between the phases 1 of the two indices. In Fig. 2b, the significant (non-significant) difference in the horizontal wind anomaly at 200 hPa is shown by the black (green) vectors. Additionally, the significant difference in the omega anomaly at 500 hPa is represented by the colored shading, while the significant difference in the H200 anomaly is depicted by the green contours. In this figure, the westerly component of the of the horizontal wind anomaly at the upper troposphere over the western half of Iran leads to an increase in the zonal wind speed at 200 hPa in the North Africa-Arabian jet exit region (6, 42). Moreover, on the northern boundaries of Iran, the negative omega anomaly, which ranges from -0.015 to -0.02 Pa s^{-1}, results in the air ascent during the phase 1 of the RM-RMM index, as compared with that of the RMM. In contrast, the air descends over the southeastern boundary of the country due to the positive omega anomaly, ranging from 0.015 to 0.02 Pa s^{-1}. In addition, in Fig. 2c, the magenta (gray) vectors denote the significant (non-significant) difference in the VIMF anomaly. In the eastern and central Iran, the significant VIMF anomaly, whose magnitude is about 21 kg $m^{-1}s^{-1}$, exhibits easterly and southeasterly directions. On the other hand, in the northwestern Iran, the southwesterlies of the VIMF anomaly possess a magnitude of about 40 kg $m^{-1}s^{-1}$. It is noteworthy that the averaged values of the significant anomalies over a region of the country has been reported in the Table-of-Fig. 2. Moreover, those values, which have been specified by an asterisk in this table, are significant at a level which is 0.05 higher than the level that has been chosen for the significance of the corresponding variable. For example, the value of the VIMF anomaly in the northwestern Iran (40 kg $m^{-1}s^{-1}$) is significant at the 0.1 level, while the values reported for this anomaly in the eastern and central part of the country are significant at the 0.05 level.

Furthermore, in Fig. 2c, the VIMFD anomaly in the northeastern, central and western Iran decreases by 1.2 mm during the phase 1 of the RM-RMM index, as compared with that of the RMM. This decrease indicates the local moisture convergence. It is noteworthy that the significant difference in the VIMFD anomaly is displayed at 0.25 level (due to the small values of the differences in this anomaly between the corresponding phases

a **OLR anom. diff.** **b** **middle to top of atmosphere**

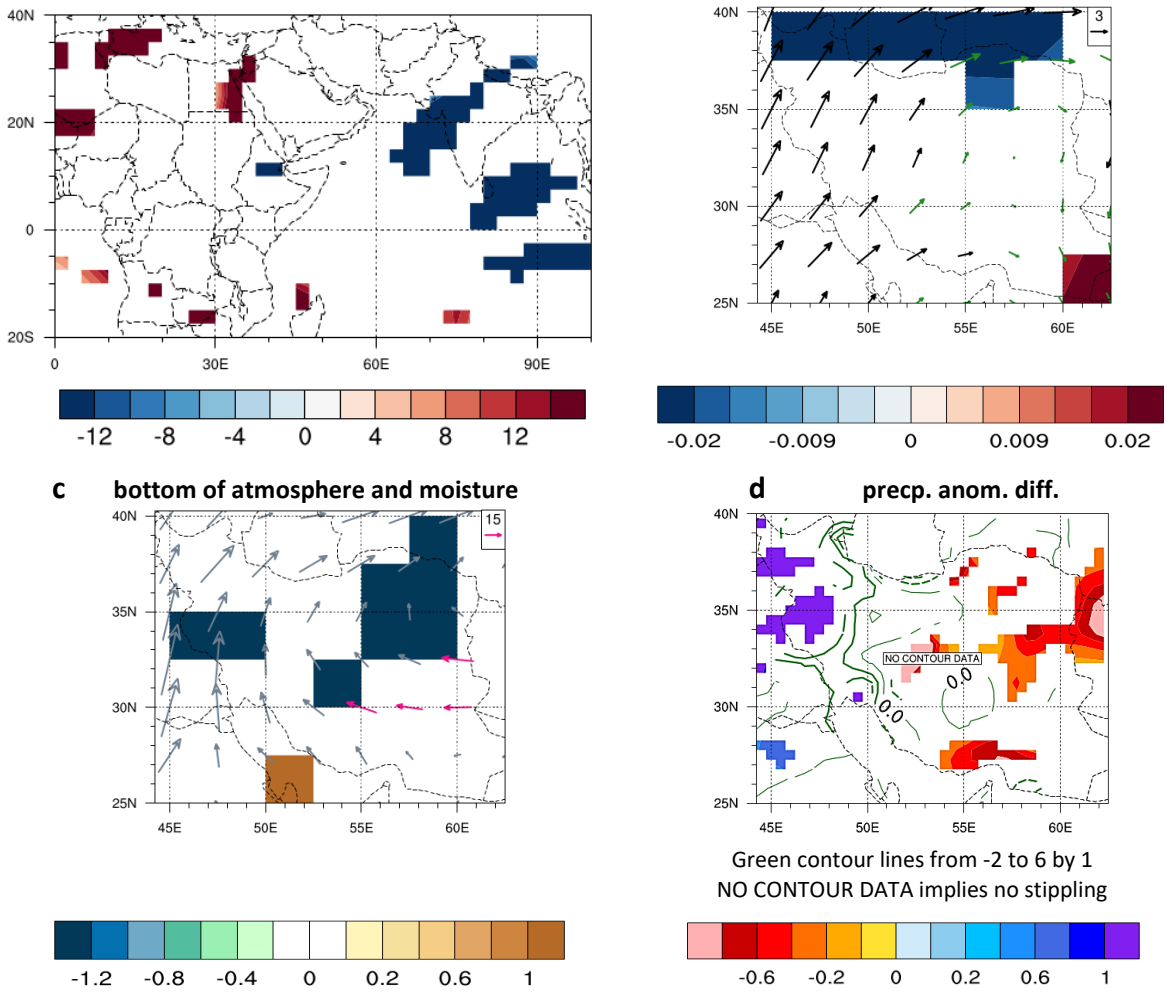

Table-of-Fig. 2	OLR	U200	H200	Omega_500	H700	VIMF	VIMFD	Precp
Northwest	-	7.5 ↗	-	-0.02	-	40* ↗	-	1
North	-	6 ↗	-	-0.02	-	-	-	-
Northeast	-	-	-	-0.017	-	-	-1.2	-0.6
West	-	6 ↗	-	-	-	-	-1.2	-
Center	-	4.5 ↗	-	-	-	20 ↖	-1.2	-0.75
East	-	-	-	-	-	22 ←	0.3*	-0.45
Southwest	-	4.5 ↗	-	-	-	-	1	-
South	-	3 ↗	-	-	-	-	-	-0.55
Southeast	-	-	-	-0.019	-	-	-	-

Fig. 2- Significant differences in various anomalies at 0.05 level (except for VIMFD which is at 0.25 level) between the phase 1 of the RM-RMM and that of the RMM index, during the +IOD event, (a) OLR anomaly (W m^{-2}), (b) 200 hPa wind vector anomaly (black vectors; m s^{-1}; green vectors indicate the non-significant differences), H200 anomaly (green contours; m), and 500 hPa omega anomaly (colored shading; Pa s^{-1}), (c) VIMF anomaly (magenta vectors; kg $m^{-1}s^{-1}$; gray vectors show the non-significant differences), H700 anomaly (black contours; m), and VIMFD anomaly (colored shading; mm), and (d) precipitation anomaly (colored shading; mm; green contours depict the non-significant differences; black stippling represents the global significance). Units are per day. The negative contours are dashed. Table of the figure shows the average of the *significant* anomalies over the *region* they occur.

of the RM-RMM and RMM indices, the significant differences might not be detected at lower levels of significance). On the contrary, in Fig. 2c, this anomaly increases by 0.8 mm over the Persian Gulf, which represents the divergence of the moisture. Finally, in Fig. 2c, no significant difference in the H700 anomaly (black contours) is

observed between the phases 1 of the RM-RMM and RMM indices.

Therefore, in the northwestern Iran, due to the air ascent, availability of significant VIMF anomaly, moisture convergence, and intensification of the sub-tropical jet at the orographic barrier, the precipitation anomaly increases by 1 mm over the Zagros Mountains during the phase 1 of the RM-RMM in comparison to the phase 1 of the RMM index (Fig. 2d). On the other hand, in some parts of the central, eastern and northeastern Iran, the precipitation anomaly decreases by 0.1 to 1 mm. The reason for this might be the lack of a significant negative OLR anomaly (cloudiness; Fig. 2a) and negative H200 anomaly (which causes instability; Fig. 2b), and, the lack of a significant anomaly of the moisture flux (Fig. 2c) in these regions. Similarly, on the southern boundary of Iran, the precipitation anomaly decreases by 0.2 to 0.8 mm during the RM-RMM phase 1 in comparison with the RMM phase 1 (Fig. 2d). In addition to the previous reasons, other reasons for this decrease might be the existence of the moisture divergence (Fig. 2c) and positive omega anomaly (Fig. 2b) in the vicinity of the Strait of Hormuz. It is noteworthy that in Fig. 2d, the significant (non-significant) difference in the precipitation anomaly is indicated by the colored shading (the green contours). Moreover, due to the lack of stippling in Fig.2d, the difference in the precipitation anomaly is not *globally* significant at the 0.05 level.

The significant differences in the anomalies between the phases 8 of the RM-RMM and RMM indices, during the +IOD event are illustrated in Fig. 3. In Fig. 3a, the OLR anomaly decreases by 10 to 12 W/m2 (see Table-of-Fig. 3) over the southern half of Iran, except for the southeastern boundaries, during the phase 8 of the RM-RMM index, as compared to that of the RMM. In Fig. 3b, the easterly component of the 200 hPa horizontal wind anomaly over the country (except for the southern and southeastern parts) weakens the sub-tropical jet. As a result, the jet exit- region is sharpened, which might be balanced by an increase in the precipitation anomaly. Moreover, the H200 anomaly is -24 m (33 m) in the northeastern (northwestern) Iran in Fig. 3b, which implies the local instability (stability), during the phase 8 of the RM-RMM index relative to the phase 8 of the RMM. Additionally, in the western, central and northern Iran, the omega anomaly at the 500 hPa level ranges from -0.015 to -0.02 Pa s^{-1}, which represents the upward motion of the air (Fig. 3b). However, this anomaly is about 0.02 Pa s^{-1} on the northeastern boundaries of the country, which indicates the air descent. In Fig. 3c, the negative H700 anomaly, which ranges from -24 to -8 m, induces instability over Iran, except for the northern and northwestern parts. Furthermore, near the core of the negative H700 anomaly, a cyclonic VIMF anomaly is observed over the western and southwestern Iran, which transports the moisture from the Persian Gulf and Sea of Oman to the southern half of the country. In addition, the northeasterlies and the easterlies of the VIMF anomaly affect the northern half of the country, except for its eastern borders. On the other hand, the VIMFD anomaly which ranges from 1 to 1.2 mm in in some parts of the northwestern, western, central, eastern and northeastern Iran, represents the moisture divergence (Fig. 3c).

Accordingly, in Fig. 3d, the precipitation anomaly increases by 0.3 to 1.5 mm in the western and central Iran during the RM-RMM phase 8 in comparison with the RMM phase 8. This might be due to the cloudiness, sharpened exit-region of the jet, uplift of the air, proximity to the minimum of the negative H700 anomaly, and, the cyclonic moisture transport to the region. Similar reasons might lead to an increase in the precipitation anomaly, ranging from the 0.2 to 0.8 mm, in the southern and southeastern Iran, although there are no significant easterlies of the U200 and negative anomaly of the 500 hPa omega on these regions. Moreover, the existence of the abundant moisture, weakened jet and upward motion of the air on the southwestern, southern and southeastern coasts of the Caspian Sea, which are restricted by the Mountains around this sea, increases the precipitation

a **OLR anom. diff.** **b** **middle to top of atmosphere**

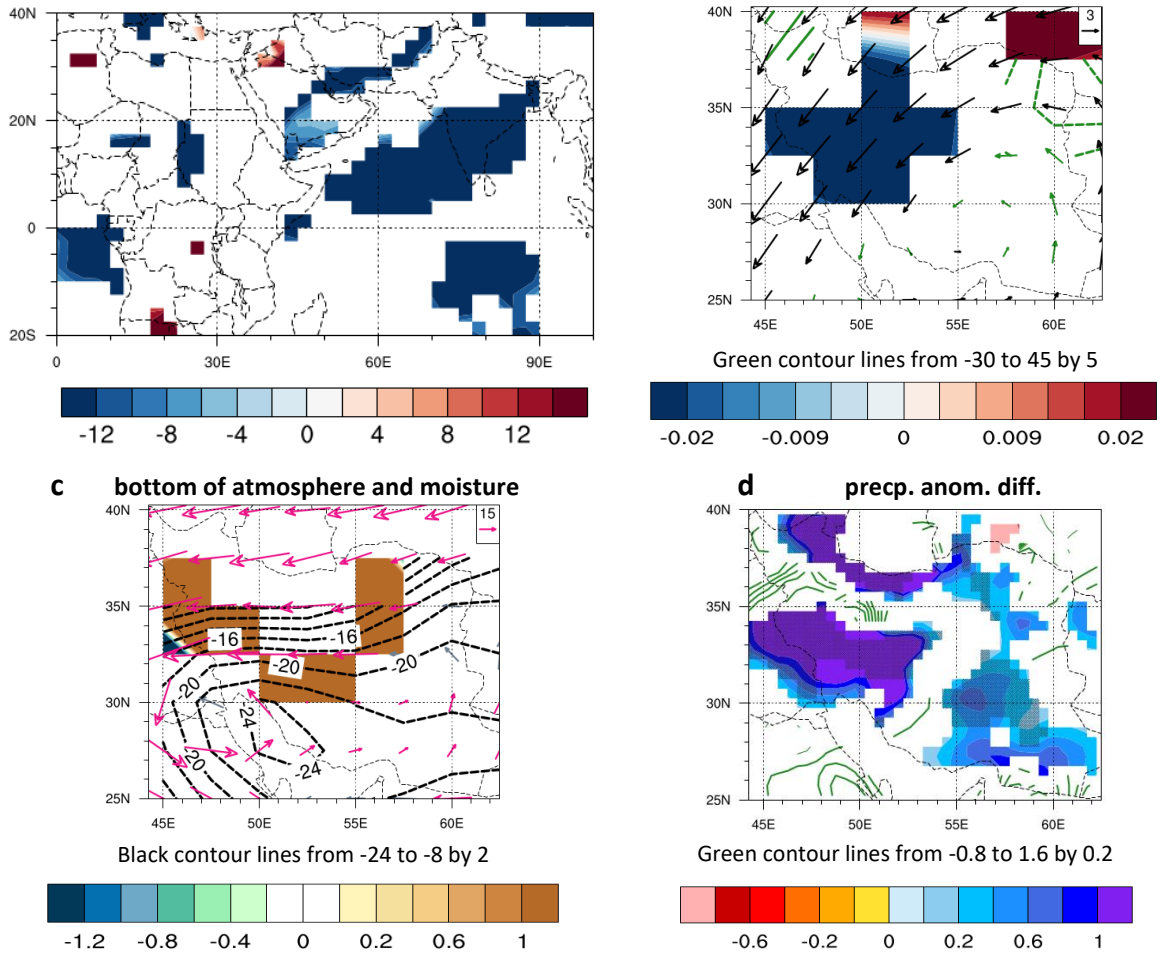

Table-of-Fig. 3	OLR	U200	H200	Omega_500	H700	VIMF	VIMFD	Precp
Northwest	-	6 ↙	33	-	-	36 ↙	1.2	0.9
North	-	7 ↙	-	-0.012	-10	37 ←	-	0.85
Northeast	-	4.2 ↙	-24	+0.02	-14	22 ↙	1.2	0.45
West	-	8 ↙	-	-0.02	-16	35 ←	1	1.2
Center	-	4.5 ↙	-	-0.02	-18	18 ←	1.2	0.6
East	-	-	-	-	-20	15* ↑	1.2*	0.4
Southwest	-11	4 ↙	-	-	-23	17 ↗	-	0.5
South	-11	1 →	-	-	-22	10 →	-	0.65
Southeast	-11	-	-	-	-20	11 ↗	-	0.65

Fig. 3- Significant differences in various anomalies between the phase 8 of the RM-RMM and that of the RMM index, during the +IOD event, as in Fig. 2

anomaly by 0.6 to 1.1 mm. Furthermore, in an area in the northeastern Iran, which is adjacent to the Caspian Sea, the instability of the air might increase the precipitation anomaly. However, due to the divergence of the moisture in this region, the precipitation anomaly experiences a lower increase, ranging from 0.2 to 0.6 mm. On the other hand, in a small area on the northeastern boundary of Iran, the precipitation anomaly decreases by 0.8 mm, which might be a consequence of both the air descent and moisture divergence in its proximity.

3.2. The Differences in Various Anomalies between the Pertinent Phases of the RM-RMM and RMM Indices during the -IOD Events

In Fig. 4a, during the occurrence of the -IOD event, the OLR anomaly decreases by -5 to -12 W/m2 (Table-of-Fig. 4) in a region on the eastern and southeastern boundaries of

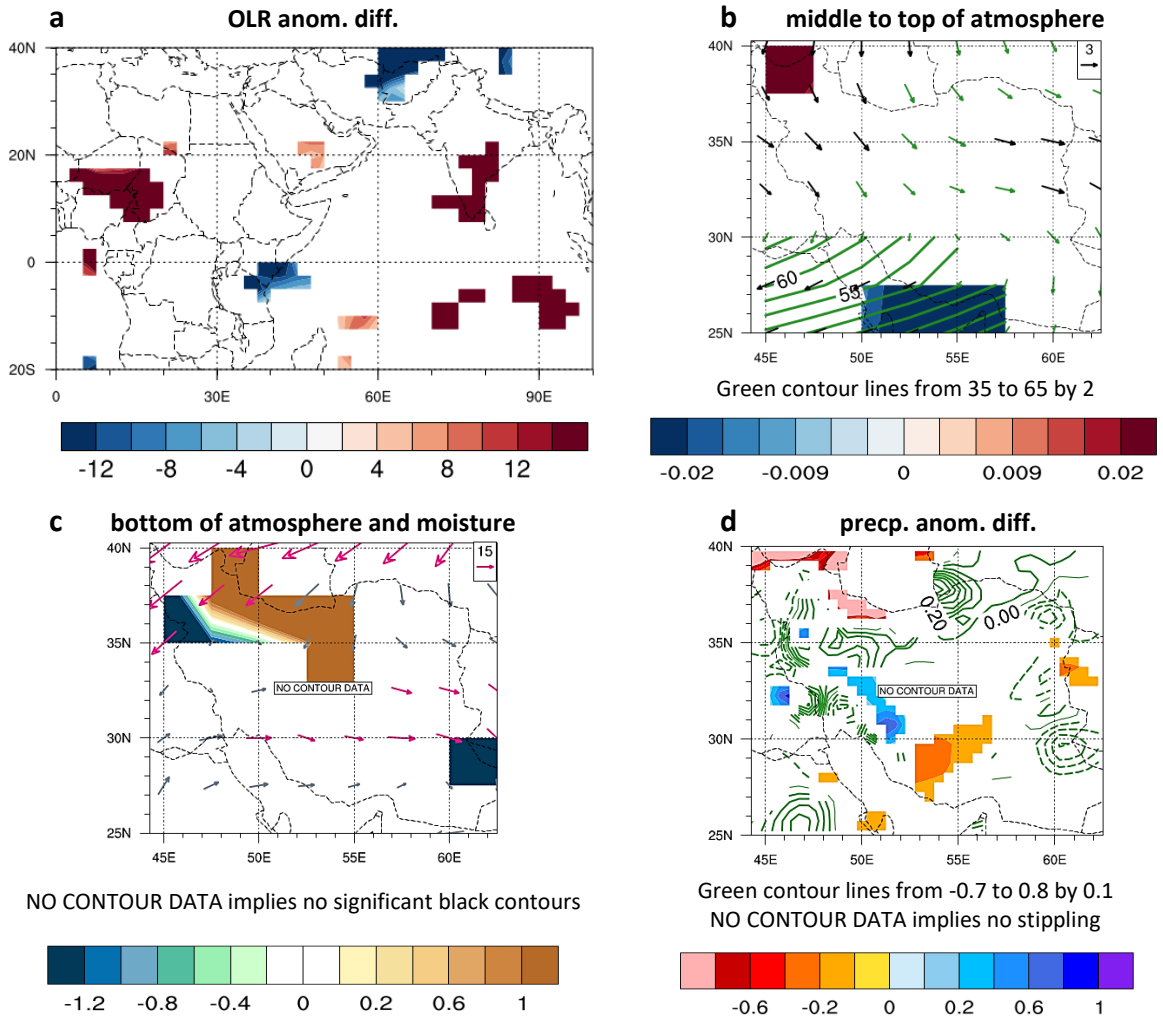

Table-of-Fig. 4	OLR	U200	H200	Omega_500	H700	VIMF	VIMFD	Precp.
Northwest	-	3.5 ↓	-	+0.02	-	36 ↙	+0.2	-0.75
North	-	4 ↘	-	-	-	-	0.8	-
Northeast	-12	4 ↘	-	-	-	-	-	-
West	-	4.25 ↘	-	-	-	20 →	-	0.3
Center	-	-	-	-	-	15 →	1*	-
East	-8	4.25 ↘	-	-	-	21 ↘	-	-
Southwest	-	2.75 ↙	57	-0.015	-	-	-	-0.14
South	-	-	45	-0.02	-	-	-	-
Southeast	-	-	-	-	-	-	-1.2	-

Fig. 4- Significant differences in various anomalies between the phase 4 of the RM-RMM and that of the RMM index, during the -IOD event, as in Fig. 2

Iran, which leads to an increase in the cloudiness during the phase 4 of the RM-RMM index, as compared to the phase 4 of the RMM. However, this anomaly is not significant in other parts of Iran. In Fig. 4b, the positive H200 anomaly ranges from 40 to 64 m in the southern and southwestern Iran, which contributes to the atmospheric stability. Additionally, at the 200 hPa level, the horizontal wind anomaly blows northerly, which does not affect the upper-level jet. On the other hand, the westerly component of the anomaly of this wind strengthens the jet in western and eastern Iran (Fig. 4b). Furthermore, the 500 hPa omega anomaly is 0.02 in the northwestern part of the country, which induces the air descent. In contrast, it is negative on the southern boundaries of Iran and results in the air ascent. In Fig. 4c, the northeasterlies of the VIMF anomaly enter the northwestern Iran. Moreover, the northwesterlies

(westerlies) of the VIMF anomaly exist over the eastern (western and central) Iran. In addition, the positive VIMFD anomaly indicates the moisture divergence (about 1 mm) over the southwestern and southern coasts of the Caspian Sea, while it ranges from 0 to -1.2 mm in a region between the northwestern and western Iran. Furthermore, this anomaly represents the convergence of the moisture (about -1.2 mm) in a small area in the southeastern Iran. It is noteworthy that the VIMF anomaly enters the western Iran from the northern part of the Persian Gulf (Fig. 4c). Moreover, in this figure, the local convergence of the moisture is observed in a region to the north of the western Iran. As a result, the intensification of the subtropical jet (Fig. 4b) increases the precipitation anomaly by 0.2 to 0.6 mm along the Zagros Mountains, as depicted in Fig. 4d. On the other hand, although the westerlies of the VIMF anomaly exist in the central Iran (Fig. 4c), there is no significant VIMF anomaly in the southwestern Iran. Furthermore, the occurrence of a large positive anomaly of H200, which stabilizes the air in the southwestern Iran (Fig. 4b), and, the divergence of the moisture in its neighborhood (in the central part of the country; Fig. 4c), leads to a decrease in the

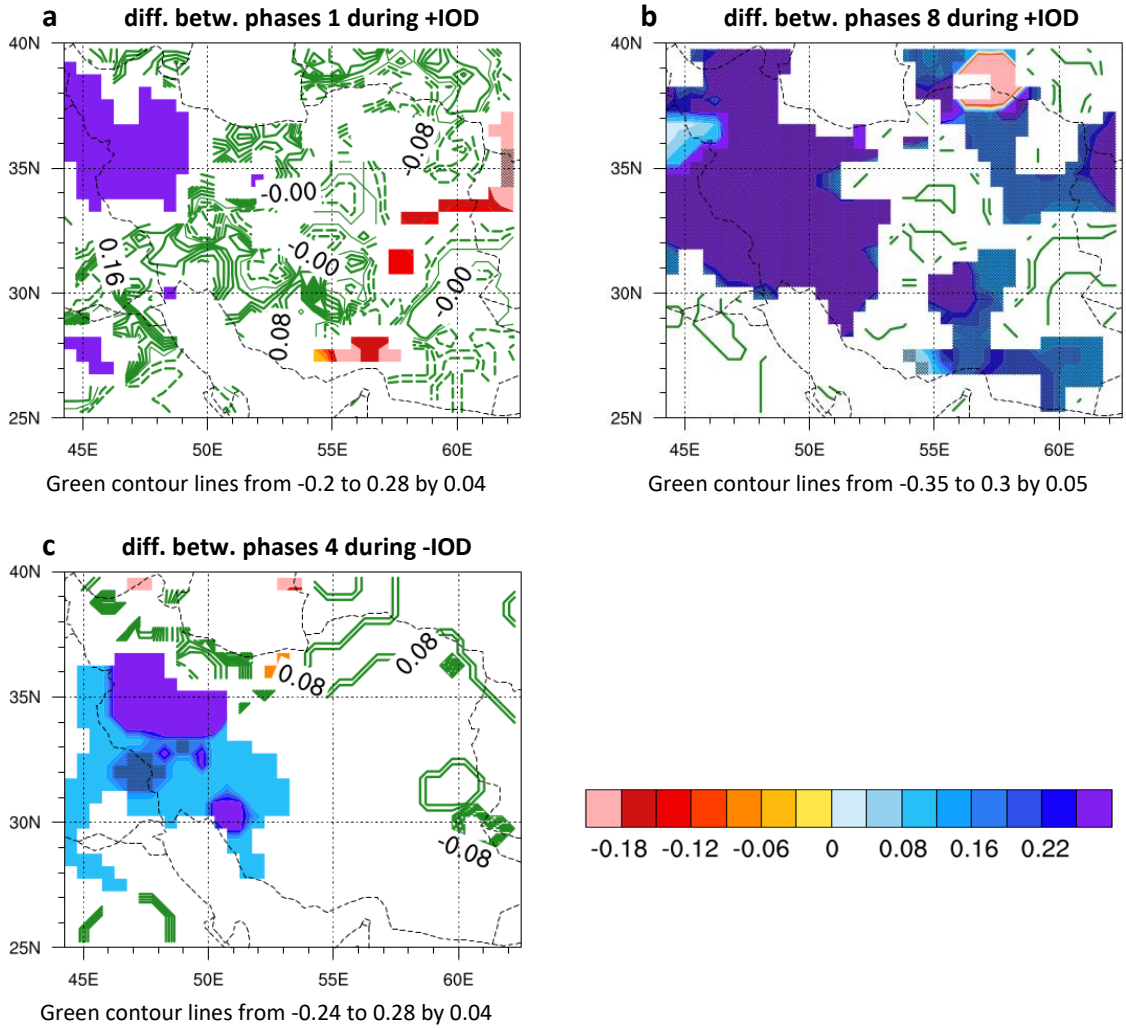

Fig. 5- Significant differences in the precipitation occurrence probability (day^{-1}) at 0.05 level between the pertinent phases of the RM-RMM and RMM indices, (a) phase 1 during the +IOD event, (b) phase 8 during the +IOD event, and (c) phase 4 during the -IOD event. Colored shading and green contours depict the locally significant and non-significant differences, respectively. Negative contours are dashed. Stippling represents the global significance at 0.05 level.

precipitation anomaly, ranging from 0.1 to 0.2, mm in the southwestern Iran (Fig. 4d). Finally, while the northeasterlies of the VIMF anomaly enter the northwestern Iran, the precipitation anomaly decreases by 0.4 to 0.8 mm in this region, due to the air descent, and the divergence of the moisture.

Fig. 5 illustrates the differences in the (average) occurrence probability of the precipitation between the pertinent phases of the RM-RMM and RMM indices during the +IOD and -IOD events, separately. In this figure, the locally significant (non-significant) differences are indicated by the colored shading (green contours). In Fig. 5a, during the +IOD event, the precipitation occurrence probability in the northwestern Iran increases by 0.28 during the phase 1 of the RM-RMM in comparison to the RMM phase 1, which is consistent with the enhanced precipitation anomaly in this region, as shown in Fig. 2d. On the contrary, in Fig. 5a, in some areas in the southern and eastern Iran the precipitation occurrence probability decreases by 0.06 to 0.21, in the phase 1 of the RM-RMM relative to the phase 1 of the RMM index.

Furthermore, in Fig. 5b, during the +IOD event, the precipitation occurrence probability increases by 0.08 to 0.28 in the northwestern, western and central Iran, and some parts of eastern half of the country, during the phase 8 of the RM-RMM in comparison with that of the RMM index. Conversely, the precipitation occurrence probability decreases by 0.2 in a small region on the northeastern boundary of Iran. These increase and decrease are consistent with those in the precipitation anomaly in Fig. 3d. On the other hand, in Fig. 5c, during the -IOD event, the precipitation occurrence probability increases by 0.07 to 0.25 in the western and central parts of the country, during the phase 4 of the RM-RMM index compared to that during the phase 4 of the RMM, in agreement with the increase in the precipitation anomaly in Fig. 4d. However, in the southern Iran no significant difference in the precipitation occurrence probability between the phases 4 of the two indices is revealed, despite the decrease in the precipitation anomaly in this area (Fig. 4d).

3.3. Discussion

According to Table 2 (sub-section 2.4), during the +IOD event, the number of the days during the MJO phases 1 and 8 is greater than that during any of the other phases (phases 2 to 7). One explanation for this observation could be the enhanced MJO activity due to the positive anomaly of the SST over the western Indian Ocean, which intensifies the convection (19, 22), and, induces the convergence of the moisture at the lower atmosphere over this region (27, 43). It is noteworthy that the phases 1 and 8 are the wet phases of the Moreover, in Table 2, the number of the days in the RMM phase 1 is greater than that in the *RMM* phase 8, during the +IOD event. This aligns with the findings reported by Jiang et al. (43), Nazemosadat et al. (18), and Sreekala et al. (21). In other words, during the +IOD event, the anomaly of the lower-level easterly winds in the equatorial Indian Ocean reduces the MJO cycle. As a reason, the negative SST anomaly over the eastern Indian Ocean induces the horizontal advection of the dry winds from the southeastern tropical Indian Ocean to its adjacent equatorial region, which might prevent from the onset of the MJO's convection and eastward propagation over the eastern Indian Ocean (44). Therefore, during the +IOD event, the convective activity of many MJOs might be suppressed after passing through the phase 3, so that the MJO terminates in the phase 3, and a new MJO emerges in the western Indian Ocean. On the contrary, in Table 2, there are more days in the phase 8 of the RM-RMM index than those in the RM-RMM phase 1, due to the 14° eastward shift of the RM-RMM index relative to the RMM. To be more precise, some of the days pertaining to the RM-RMM phase 8, coincide with the RMM phase 1 - which possesses the largest number of days among the RMM phases. As a result, the days associated to the RM-RMM phase 8 increases, in comparison to those belonging to the RMM phase 8. Consistently, in Fig. 3d (Fig. 5b), the amount of the precipitation anomaly (occurrence probability) during the phase 8 of the RM-RMM index increases over a wide region in Iran compared to the phase 8 of the RMM. It is worth mentioning that a

similar discussion might justify the significant increase in the precipitation variation over the northwestern Iran during the phase 1 of the RM-RMM index relative to the RMM phase 1, as depicted in Fig. 2d and Fig. 5a. However, on some small parts in the southern, eastern and northeastern Iran, the precipitation variabilities decrease during the RM-RMM phase 1 with respect to the RMM phase 1, due to the lack of a significant difference in the VIMF anomaly (Fig. 2d and Fig. 5a).

In Table 3, it is observed that during the -IOD event, the maximum number of the days occurs during the phases 4 to 6, specifically during the phase 5, that the MJO activity is over the Maritime Continent (the dry phase of the MJO over the southwestern Asia). This is attributed to the anomalous westerly winds at the lower troposphere and the increased moisture flux anomaly over the eastern tropical Indian Ocean during the -IOD event (19, 43). These conditions lead to the strengthening of the MJO's convective activity over this region. Therefore, the number of the days which belong to the phases 4 to 6 increases, regardless of whether the MJO has been classified as active or weak during the phase 1 at the beginning of its cycle. This finding is consistent with the results presented by Jiang et al. (43).

In a similar manner to the +IOD case, during the -IOD event (Table 3), the largest relative difference (sub-section 2.4) in the number of the days between the corresponding phases of the RM-RMM and RMM indices is observed during the phase 4. Again, this might be due to the 14° phase-shift of the RM-RMM in comparison with the RMM index. In other words, some of the days of the RM-RMM phase 4 coincide with the phase 5 of the RMM index, which possesses the greatest number of days among the RMM phases. As a result, a significant decrease in the precipitation anomaly is evident over the southwestern Iran during the phase 4 of the RM-RMM index compared to the phase 4 of the RMM (Fig. 4d). It is noteworthy that during the phases 4 and 5 of the RMM, the -IOD event might enhance the suppression of the MJO's convection over the western Indian Ocean, due to the negative anomaly of the SST and lower-level divergence of the moisture in this region. As a result, the precipitation over the southwestern Asia might decrease during these MJO phases. However, during the phase 4 of the RM-RMM index, the precipitation variabilities increase over a part of the western Iran compared to that of the RMM. This is attributed to the presence of a significant moisture anomaly, proximity to a region of local moisture convergence, and, intensification of the sub-tropical jet at the orographic barrier of the Zagros Mountains (Fig. 4d and Fig. 5c).

4. Summary and Conclusions

As the IOD might affect the precipitation over a region by modulating the MJO, in the current study, to improve the estimate of the IOD influence on the MJO-related precipitation variabilities over Iran, each of the (concurrently) active phase numbers of the RM-RMM and RMM indices is subdivided into three subsets, based on the IOD state (+IOD, Neutral IOD, and -IOD) during the ON months of 1979 to 2022, which coincide with the peak activity of the IOD. Subsequently, the significant differences in the precipitation anomaly (precipitation occurrence probability) between the corresponding phases of the RM-RMM and RMM indices are revealed over Iran during the +IOD and the -IOD events. However, no significant differences in the precipitation variations between the equivalent phases of the two indices are observed across the country during the Neutral IOD event.

During the +IOD event, the convergence of the moisture at the lower troposphere and enhancement of the convection activity of the MJO due to the positive SST anomaly over the western Indian Ocean result in an increase in the precipitation variations in this region during the phases 8 and 1 of the MJO. The 14° eastward phase-shift of the RM-RMM phase (relative to the RMM index) allows it to capture this enhanced activity more effectively than the RMM index. Accordingly, due to the cloudiness, uplift of the air, cyclonic advection of the moisture and sharpened exit-region of the upper-level jet the precipitation anomaly (occurrence probability) increases by 0.1 to 1.5 mm (0.08 to 0.28) in the western, central, southern, southeastern and northeastern Iran, and, on

the southwestern, southern and southeastern coasts of the Caspian Sea, during the phase 8 of the RM-RMM in comparison with that of the RMM. On the contrary, in a small area on the northeastern boundary of Iran, the air descent and moisture divergence lead to a decrease in the precipitation anomaly (occurrence probability), which is about 0.8 mm (0.2).

In addition, the existence of a significant VIMF anomaly, air ascent, and intensification of the jet at the upper troposphere, increase the precipitation anomaly (occurrence probability) by 1 mm (0.28) over the Zagros Mountains in the northwestern Iran, during the phase 1 of the RM-RMM index compared to the phase of the RMM. However, the lack of a significant VIMF anomaly causes a decrease in the precipitation anomaly (occurrence probability), ranging from 0.1 to 1 mm (0.06 to 0.21), on some small parts in the southern, eastern and northeastern Iran, during the RM-RMM phase 1 with respect to the RMM phase 1.

On the other hand, during the -IOD event, the negative SST anomaly weakens the MJO's convection over the western Indian Ocean. Moreover, the divergence of the moisture at the lower troposphere on this region takes place. These factors might result in a decrease in the precipitation anomaly during the phase 4 (dry phase) of the MJO over the southwestern Asia. The RM-RMM index captures this signal more effectively than the RMM index due to its 14° eastward phase-shift. In this manner, the air subsidence and the lack of a significant VIMF anomaly decreases the precipitation anomaly by 0.1 to 0.2 mm over the southwestern Iran, during the RM-RMM phase 4 relative to the RMM phase 4. However, due to the intensification of the sub-tropical jet in the vicinity of the regions, over which the significant moisture anomaly and local moisture convergence exists, the precipitation anomaly (occurrence probability) increases by 0.2 to 0.6 mm (0.07 to 0.25) over the Zagros Mountains in the western Iran, during the phase 4 of the RM-RMM index compared to that of the RMM.

In conclusion, these findings suggest that by predicting the interannual variations of the IOD, and considering the significant differences between the corresponding phases of the RM-RMM and RMM indices, the estimation of the influence of IOD on the MJO-related precipitation over Iran might be ameliorated. In other words, there is potential for enhancing the accuracy of the long-range precipitation forecasts, which is consistent with the results of Roundy et al. (45).

Conflict of interest

The author declares that he has no conflict of interest.

5. References

1. Madden, R.A., and Julian, P.R. (1972). Description of global-scale circulation cells in the tropics with a 40–50 day period. Journal of Atmospheric Sciences, 29, 1109-1123.
2. Hoskins, B., and Karoly, D. (1981). The steady linear response of a spherical atmosphere to thermal and orographic forcing. Journal of Atmospheric Sciences, 38, 1179-1196.
3. Seo, K.H., and Son, S.W. (2012). The global atmospheric circulation response to tropical diabatic heating associated with the Madden–Julian Oscillation during northern winter. Journal of Atmospheric Sciences, 69, 79-96.
4. Seo, K.H., and Lee, H.J. (2017). Mechanisms for a PNA-like teleconnection pattern in response to the MJO. Journal of Atmospheric Sciences, 74, 1767-1781.
5. Lee, H.J., and Seo, K.H. (2019). Impact of the Madden-Julian oscillation on Antarctic sea ice and its dynamical mechanism. Scientific Reports, 9, 10761.
6. Cannon, F., Carvalho, L.M.V., Jones, C., Hoell, A., Norris, J., Kiladis, G.N., and Tahir, A.A. (2017). The influence of tropical forcing on extreme winter precipitation in the western Himalaya. Climate Dynamics, 48, 1213-1232.
7. Moore, R.W., Martius, O., and Spengler, T. (2010). The modulation of the subtropical and extratropical atmosphere in the Pacific basin in response to the Madden-Julian

oscillation. Monthly Weather Review, 138, 2761–2779.
8. Stan, C., Straus, D.M., Frederiksen, J.S., Lin, H., Maloney, E.D., and Schumacher, C. (2017). Review of tropical-extratropical teleconnections on intraseasonal time scales. Reviews of Geophysics, 55, 902-937.
9. Straus, D.M., Swenson, E., and Lappen, C.-L. (2015). The MJO cycle forcing of the North Atlantic Circulation: Intervention experiments with the Community Earth System Model. Journal of Atmospheric Sciences, 72, 660-681.
10. Wheeler, M.C., and Hendon, H.H. (2004). An all-season real-time multivariate MJO index: Development of an index for monitoring and prediction. Monthly Weather Review, 132, 1917-1932.
11. Hoell, A., Cannon, F., and Barlow, M. (2018). Middle East and Southwest Asia daily precipitation characteristics associated with the Madden–Julian Oscillation during boreal winter. Journal of Climate, 31, 8843-8860.
12. Schreck, C.J. III. (2021). Global survey of the MJO and extreme precipitation. Geophysical Research Letters, 48, e2021GL094691.
13. Zhang, C. (2013). Madden–Julian Oscillation: Bridging weather and climate. Bulletin of the American Meteorological Society, 94, 1849-1870.
14. Mansouri, S., Masnadi-Shirazi, M. A., Golbahar-Haghighi, S., and Nazemosadat, M. J. (2021). An analogy toward the real-time multivariate MJO Index to improve the estimation of the impacts of the MJO on the precipitation variability over Iran in the Boreal Cold Months. Asia-Pacific Journal of Atmospheric Sciences, 57, 207–222.
15. Hoell, A., Shukla, S., Barlow, M., Cannon, F., Kelley, C., and Funk, C. (2015). The forcing of monthly precipitation variability over Southwest Asia during the boreal cold season. Journal of Climate, 28, 7038-7056.
16. Matthews, A.J. (2008), Primary and successive events in the Madden–Julian Oscillation. Quarterly Journal of the Royal Meteorological Society., 134: 439-453.
17. Nazemosadat, M.J., Shahgholian, K., Ghaedamini, H., and Nazemosadat, E. (2021). Introducing new climate indices for identifying wet/dry spells within a Madden-Julian Oscillation phase. International Journal of Climatology, 41 (Suppl. 1), E1686–E1699.
18. Nazemosadat, M.J., Shahgholian, K., and Ghaedamini, H. (2023). The wet and dry spells within the MJO-phase 8 and the role of ENSO and IOD on the modulation of these spells: a regional to continental-scales analysis. Atmospheric Research, 285, 106631.
19. Wilson, E.A., Gordon, A.L., and Kim, D. (2013). Observations of the Madden Julian oscillation during Indian ocean dipole events. Journal of Geophysical Research: Atmospheres, 118, 2588–2599.
20. Saji, N.H., Vinayachandran, P.N., and Yamagata, T. (1999). A dipole mode in the tropical Indian Ocean. Nature, 401, 360–363.
21. Sreekala, P.P., Rao, S.V.B., Rajeevan, K., and Arunachalam, M.S. (2018). Combined effect of MJO, ENSO and IOD on the intraseasonal variability of northeast monsoon rainfall over south peninsular India. Journal of Climate, 51, 3865–3882.
22. Kug, J.S., Sooraj, K.P., Jin, F.F., Lou, J.J., and Kwon, M. (2009). Impact of Indian Ocean Dipole on high-frequency variability over the Indian Ocean. Atmospheric Research, 94(1), 134–139.
23. Shinoda, T., and Han, W. (2005). Influence of the Indian Ocean Dipole on atmospheric subseasonal variability. Journal of Climate, 18, 3891–3909.
24. Pourasghar, F., Oliver, E.C.J., and Holbrook, N.J. (2019). Modulation of wet-season rainfall over Iran by the Madden–Julian Oscillation, Indian Ocean Dipole and El Niño–Southern Oscillation. International Journal of Climatology, 39, 4029–4040.
25. Nazari-Radsani, M., Vatanparast-Ghaleh-Jouq, F., Nazemosadat, M., and Salahi, B. (2021). Effects of Pure and Combined Events of ENSO and IOD Phenomena on Autumn Precipitation Variations in the

Northwest Iran. Journal of Meteorology and Atmospheric Sciences, 4(3): 193-209. [In Persian].
26. Pourasghar, F., Tozuka, T., Jahanbakhsh, S., Sari Sarraf, B., Ghaemi, H., and Yamagata, T. (2012). The interannual precipitation variability in the southern part of Iran as linked to large-scale climate modes. Climate Dynamics, 39, 2329–2341.
27. Tuel, A., Choi, Y., AlRukaibi, D., and Eltahir, E. (2022). Extreme storms in southwest asia (northern arabian peninsula) under current and future climates. Climate Dynamics, 58, 1509-1524.
28. Salby, M.L., and Hendon, H.H. (1994). Intraseasonal behavior of clouds, temperature and motion in the Tropics. Journal of Atmospheric Sciences, 51, 2207–2224.
29. Chen, M., Shi, W., Xie, P., Silva, V.B.S., Kousky, V.E., Higgins, R.W., and Janowiak, J.E. (2008). Assessing objective techniques for gauge-based analyses of global daily precipitation. Journal of Geophysical Research, 113, D04110.
30. Kalnay, E., and Coauthors (1996). The NCEP/NCAR 40-year reanalysis project. Bulletin of the American Meteorological Society, 77, 437-472.
31. Krishnamurthy, V., and Shukla, J. (2000). Intraseasonal and interannual variability of rainfall over India. Journal of Climate, 13, 4366-4377.
32. Efron, B., and Tibshirani, R. (1993). An Introduction to the Bootstrap. Boca Raton, FL: Chapman and Hall.
33. Ventura, V., Paciorek, C.J., and Risbey, J.S. (2004). Controlling the proportion of falsely rejected hypotheses when conducting multiple tests with climatological data. Journal of Climate, 17, 4343-4356.
34. Wilks, D.S. (2006). On "field significance" and the false discovery rate. Journal of Applied Meteorology and Climatology, 45, 1181-1189.
35. Wilks, D.S. (2016). "The stippling shows statistically significant grid points": How research results are routinely overstated and over-interpreted, and what to do about it. Bulletin of the American Meteorological Society, 97, 2263-2273.
36. Gloeckler, L.C., and Roundy, P.E. (2019). A statistical analysis of relationships between western North Pacific tropical cyclones and extratropical circulation patterns accompanying the Madden–Julian Oscillation. Journal of Atmospheric Sciences, 76, 583-604.
37. Liebmann, B., and Smith, C.A. (1996). Description of a Complete (Interpolated) Outgoing Longwave Radiation Dataset. Bulletin of the American Meteorological Society, 77, 1275-1277.
38. Gottschalck, J., Wheeler, M., Weickmann, K., Vitart, F., Savage, N., Lin, H., ... and Higgins, W. (2010). A framework for assessing operational Madden–Julian Oscillation forecasts: a CLIVAR MJO Working Group Project. Bulletin of the American Meteorological Society, 91, 1247-1258.
39. Raziei, T., Daneshkar Arasteh, P., and Saghafian, B. (2005). Annual Rainfall Trend Analysis in Arid and Semi-arid Regions of Central and Eastern Iran. Journal of Water and Wastewater, 16(2), 73-81. [In Persian].
40. Nazemosadat, M. J., and Ghasemi, A. R. (2004). Quantifying the ENSO-Related Shifts in the Intensity and Probability of Drought and Wet Periods in Iran. Journal of Climate, 17, 4005–4018.
41. Guo, B., and Yuan, Y. (2015). A comparative review of methods for comparing means using partially paired data. Statistical Methods in Medical Research, 26(3):1323-1340.
42. Barlow, M., Wheeler, M., Lyon, B., and Cullen, H. (2005). Modulation of daily precipitation over Southwest Asia by the Madden-Julian Oscillation. Monthly Weather Review, 133, 3579-3594.
43. Jiang, Y., Zhou, L., Roundy, P.E., Hua, W., and Raghavendra, A. (2021). Increasing influence of Indian Ocean Dipole on precipitation over Central Equatorial Africa. Geophysical Research Letters, 48, e2020GL092370.
44. Seiki, A., Nagura, M., Hasegawa, T., and Yoneyama, K. (2015). Seasonal Onset of the Madden–Julian Oscillation and its Relation to the Southeastern Indian Ocean Cooling. Journal of the

Meteorological Society of Japan, 93A, 139-156.

45. Roundy, P. E., MacRitchie, K., Asuma, J., and Melino, T. (2010). Modulation of the global atmospheric circulation by combined activity in the Madden-Julian oscillation and the El Niño-Southern oscillation during boreal winter. Journal of Climate, 23, 4045–4059.